CrossMark

Quantification of the impact of TOF and PSF on PET images using the noise-matching concept: clinical and phantom study

M. Shekari[1,2] · P. Ghafarian[3,4] · S. Ahangari[1,2] · M. R. Ay[1,2]

Abstract This study was to assess quantitatively the accuracy of ^{18}F-FDG PET/CT images reconstructed by TOF + PSF and TOF only, considering the noise-matching concept to minimize probable bias in evaluating algorithm performance caused by noise. PET images of similar noise level were considered. Measurements were made on an in-house phantom with hot inserts of Φ10–37 mm, and oncological images of 14 patients were analyzed. The PET images were reconstructed using the OSEM, OSEM + TOF and OSEM + TOF + PSF algorithms. Optimal reconstruction parameters including iteration, subset, and FWHM of post-smoothing filter were chosen for both the phantom and patient data. In terms of quantitative accuracy, the recovery coefficient (RC) was calculated for the phantom PET images. The signal-to-noise ratio (SNR), lesion-to-background ratio (LBR), and SUV_{max} were evaluated from the phantom and clinical data. The smallest hot insert (Φ10 mm) with 2:1 activity concentration ratio could be detected in the PET image reconstructed using the TOF and TOF + PSF algorithms, but not the OSEM algorithm. The relative difference for SNR between the TOF + PSF and OSEM showed significantly higher values for smaller sizes, while SNR change was smaller for Φ22–37 mm inserts both 2:1 and 4:1 activity concentration ratio. In the clinical study, SNR gains were 1.6 ± 0.53 and 2.7 ± 0.74 for the TOF and TOF + PSF, while the relative difference of contrast was 17 ± 1.05 and 41.5 ± 1.85% for the TOF only and TOF + PSF, respectively. The impact of TOF + PSF is more significant than that of TOF reconstruction, in smaller inserts with low activity concentration ratio. In the clinical PET/CT images, the use of the TOF + PSF algorithm resulted in better SNR and contrast for lesions, and the highest SUV_{max} was also seen for images reconstructed with the TOF + PSF algorithm.

✉ P. Ghafarian
   pardis.ghafarian@sbmu.ac.ir

1   Department of Medical Physics and Biomedical Engineering, Tehran University of Medical Sciences, Tehran, Iran

2   Research Center for Molecular and Cellular Imaging, Tehran University of Medical Sciences, Tehran, Iran

3   Chronic Respiratory Diseases Research Center, National Research Institute of Tuberculosis and Lung Diseases (NRITLD), Shahid Beheshti University of Medical Sciences, Tehran, Iran

4   PET/CT and Cyclotron Center, Masih Daneshvari Hospital, Shahid Beheshti University of Medical Sciences, Tehran, Iran

1 Introduction

PET/CT imaging using ^{18}F-fluorodeoxyglucose (FDG) is widely used in oncology for diagnosis, staging, restaging of disease and patient management. Image quality of FDG PET is important for accurate cancer diagnosis and assessing response to therapy [1–3]. PET/CT images can be assessed quantitatively by the use of parameters of the signal-to-noise ratio (SNR) and lesion-to-background ratio (LBR), and semiquantitative parameters of recovery coefficient and standard uptake value [4]. Maximum

🍩 Springer

standardized uptake value (SUVmax) is commonly used in clinical studies to evaluate malignant lesions [5].

Studies show that reconstruction parameters can affect significantly the quantitative analysis [6–9]. Due to advent of new fast scintillators, electronic improvements, emergence of cheaper computing power, and the reconstruction methods, today time of flight (TOF) and point spread function (PSF) are implemented in clinical PET image reconstruction, with improved image quality [10–16]. PSF improves the spatial resolution, minimizes the partial volume effect, and increases SNR in PET images [11, 17]. Lesion detectability and SNR can be increased by incorporating the TOF method [18–23]. Further improvement in PET/CT image quality can be made by combining the TOF and PSF algorithms in the reconstruction process [6, 19, 24–28]. Using PSF + TOF algorithm, lesion detectability and SUV of lymph nodes can be better shown than using conventional OSEM (ordered subset expectation–maximization) algorithm in PET/CT images [29, 30]. Recently, Prieto et al. [29] demonstrated that incorporation of the PSF with TOF was an optimal method for quantification of small lesion.

Accurate quantitative analysis is essential for therapy monitoring. On basis of our previous study and the noise-matching concept, the TOF and TOF + PSF are compared with the OSEM algorithm using a phantom with hot inserts of Φ10–37 mm and activity concentration ratios of 2:1 and 4:1 [16, 31]. Clinical PET/CT images were evaluated quantitatively and qualitatively.

2 Experimental section

2.1 Phantom study

PET/CT images were evaluated by a phantom created in-house, having six fillable cylindrical inserts in diameters of 10, 13, 17, 22, 28, and 37 mm, and a lung insert, placed in a body compartment. The body compartment is similar to NEMA image quality phantom, with the same shape and dimensions. The body phantom was filled with an ^{18}F-FDG solution of 5.3 kBq/mL activity concentration that was equivalent to liver uptake of a 70 kg patient received 370 MBq intravenous ^{18}F-FDG [32]. All inserts were filled with 2:1 and 4:1 activity concentration ratios, to compare with background activity concentration of ^{18}F-FDG solution separately.

2.2 Patient study

A retrospective analysis was made for 14 oncological patients (8 men and 6 women) who had undergone ^{18}F-FDG PET/CT examination. The clinical indications for the patients were the evaluation of lung cancer ($n = 4$), colon cancer ($n = 3$), breast cancer ($n = 3$), renal cell carcinoma ($n = 2$), and gastric cancer ($n = 2$). Patients with liver lesions or with a fasting blood sugar level higher than 150 mg/dL were excluded in our investigation. All patients fasted 6–8 h before the PET/CT examination. The patients weighed in average 78.5 ± 3.8 kg (65–90 kg) and received an intravenous injection of 320.2 ± 19.3 MBq of ^{18}F-FDG (279–406 MBq) according to EANM (European Association of Nuclear Medicine) guidelines [33]. The PET/CT scan was obtained 61.1 ± 1.7 min post-injection.

2.3 Data acquisition and reconstruction parameters

In this study, we used a Discovery 690 VCT (GE Healthcare, Milwaukee, USA) with lutetium-yttrium oxy-orthosilicate (LYSO) crystal combined with a 64-slice CT scanner. The PET scanner has a timing resolution of 555 ps with a 4.9-ns coincidence time window. It consists of 24 rings and a total of 13824 LYSO crystals, each being sized at 4.2 mm × 6.2 mm × 25 mm. The PET scanner covers 15.7 cm axial field of view and trans-axial field of view (FOV) is 70 cm in diameter. After performing a CT topogram, the CT images acquired using smart mA technique depending on body habitus from vertex to mid-thigh with tube voltage of 100–120 kVp (depending on patient size), pitch of 0.98:1, 1-s gantry rotation time, and 3.75-mm slice thickness.

The PET images were acquired in list mode with 3 min per bed position. All images reconstructed with the OSEM (commercially termed as VUE.HD), OSEM + TOF (TOF, commercially VUE.FX), and OSEM + TOF + PSF (TOF + PSF, manufactured standard full name as Sharp-IR) algorithms, with image matrix of 256 × 256 (pixel size, 2.73 mm) [34, 35]. Based on our previous study and the noise-matching concept [27, 31], reconstruction parameters were chosen for the clinical and phantom studies. In other words, reconstruction parameters of iteration, subset, and FWHM of post-smoothing filter were chosen to achieve noise level (defined as coefficient of variance) lower than 10% for both phantom and clinical images. In the phantom study, reconstruction parameters were 2 iterations and 24 subsets for reconstructions with the TOF and TOF + PSF method and 3 iterations and 24 subsets for the OSEM method. Full width at half maximum (FWHM) of Gaussian filter was 6, 5.5, and 4 mm for the OSEM, TOF, and TOF + PSF algorithms, respectively. Clinical PET images were reconstructed with 2 iterations and 18 subsets for the TOF method and 3 iterations and 18 subsets for the OSEM algorithm. FWHM of applied Gaussian filters was 6.4, 5.5, and 4 mm for the OSEM, TOF, and TOF + PSF algorithms, respectively. The noise level for all phantom images was 8.5 ± 0.3%, and all

clinical PET images had the noise level of 7.78 ± 0.5%, regardless of reconstruction method used.

2.4 Assessment strategy

For evaluation of image quality and quantitative analysis for PET/CT images in the phantom and clinical studies, the coefficient of variation (COV) was calculated based on the noise-matching concept [27]. For the phantom images, 12 circular ROIs (region of interest) were drawn on central slices and ± 2 slices away, resulting a total of 60 ROIs in the background (Uniform area) [36]. For clinical PET images, liver due to uniform uptake was considered as background and the COV was measured by drawing 3 spherical VOIs (Φ37 mm) on the 3 axial slices in the largest and uniform liver section (9 VOIs) that did not cover the porta-hepatis and any of the major vessels in the liver [33].

COV was defined as the mean average activity concentration to the standard deviation of all drawn ROIs for the phantom and clinical images. SNR, lesion-to-background ratio (LBR), and SUVmax were evaluated. SNR was measured as the ratio of the maximum value of tracer activity concentration within a drawn VOI involving the lesion minus the mean activity concentration in background over the SD in the background, and LBR was calculated as the ratio of the maximum value of a VOI involving the lesion over the mean value in the background. For the image quality phantom with 2:1 and 4:1 activity concentration ratios, the accuracy of measured activity concentration was determined as the recovery coefficient (RC) for all the hot inserts. RC was defined as the ratio of observed activity concentration at 50% of 3D isocontour to true activity concentration, multiplied by 100.

In clinical data, based on guidelines recommendation, lesion size was estimated by drawing a 3D isocontour at 50% maximum voxel values over a lesion in the images reconstructed with the OSEM algorithm [33]. For TOF and TOF + PSF, relative changes in SNR with respect to the OSEM method were calculated by: $\Delta SNR = [(SNR - SNR_{OSEM})/SNR_{OSEM}] \times 100\%$, where SNR is the calculated SNR of the TOF or TOF + PSF images, and SNR_{OSEM} is the measured SNR for images reconstructed with the OSEM algorithm. Relative changes were calculated, too, for other quantitative parameters including SUV_{max} and contrast in the TOF and TOF + PSF method compared to the OSEM algorithm. SNR gain, defined as the ratio of lesion SNR in images reconstructed with the TOF or TOF + PSF method to the corresponding SNR in the OSEM images, was calculated for clinical images. Relative difference of RC was evaluated with regard to insert of Φ10–37 mm in both activity concentration ratios. The different methods were compared by box and whisker plot, Bland–Altman plots (using a 95% confidence interval), and linear regression analysis. Quantitative analysis was done by two expert radiologist and nuclear medicine physicians.

2.5 Statistical analysis

Normal distribution of each variable was evaluated by Shapiro–Wilk analysis. Most of variables rejected normal distribution which guaranteed using parametric analysis. All quantitative parameters were evaluated by nonparametric tests. In addition, Spearman's correlation coefficient was used for pairwise comparison. Significance level within 95% confidence interval was defined as 0.05 for all comparisons. Statistical analysis was done by SPSS package (SPSS, version 22.0, Armonk, NY).

3 Results

Reconstructed images of the phantom with 2:1 and 4:1 activity concentration ratios and background activity concentration of 5.3 kBq/mL are shown in Fig. 1. Comparing with HD images, quality of the TOF and TOF + PSF algorithm was improved obviously for both activity concentration ratios, especially images reconstructed with the TOF + PSF method. At activity concentration ratio of 2:1, the 10-mm hot insert is visible in the TOF and TOF + PSF images, but not in the HD image.

Table 1 shows the recovery coefficients at LBR = 2:1 and 4:1 for images of the phantom inserts of Φ10–37 mm, reconstructed with the three methods. In general, RC increased with insert diameter for all algorithms and activity concentration ratios, and the greatest values were achieved by the TOF + PSF algorithm. At LBR = 4:1, the relative difference between the TOF + PSF and OSEM method was 23.2% at Φ13 mm, and 8.2% at Φ37 mm.
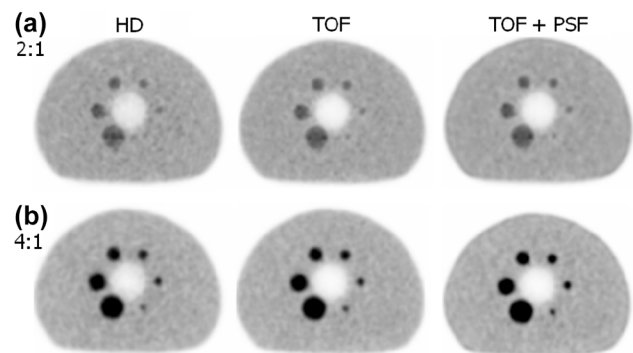

Fig. 1 PET images of phantoms reconstructed with the algorithms at 5.3 kBq/mL background activity concentration and LBR = 2:1 (**a**) and 4:1 (**b**)

Table 1 Recovery coefficient (*RC*) and relative difference of *RC* for TOF and TOF + PSF compared to OSEM algorithm

Phantom diameter (mm)	RC%						ΔRC%			
	HD		TOF + PSF		TOF		TOF		TOF + PSF	
	2:1	4:1	2:1	4:1	2:1	4:1	2:1	4:1	2:1	4:1
10	ND	50.9	70.6	51.6	71.6	60.1	NM	1.4	NM	18.0
13	83.1	59.9	84.5	62.1	87.7	73.8	1.7	3.7	5.6	23.2
17	90.5	66.7	91.4	69.9	100.3	80.3	1.0	4.9	10.8	20.4
22	99.2	73.0	98.6	75.5	105.9	83.2	− 0.7	3.4	6.7	14.0
28	104.1	76.2	102.6	79.6	109.4	85.3	− 1.4	4.4	5.1	11.9
37	108.9	82.2	110.4	83.2	115.9	89.0	1.4	1.2	6.5	8.2

ND not detected; *NM* not measured

SNR increased with insert diameter, too, for all reconstruction methods and activity concentration ratios (Fig. 2a), while the relative difference of SNR, between the TOF + PSF and OSEM, decreased with increasing diameters, for both activity concentration ratios. Figure 2b shows the SUV_{max} for each hot insert reconstructed with the algorithms for LBR = 4:1 and 2:1.

The difference for SNR and SUV_{max} was measured for the inserts (Table 2). Due to the performance of the PSF algorithm in partial volume effect correction specially in small lesions in parallel with signal enhancement by the TOF algorithm, there were significant SNR improvements for hot inserts of Φ10–17 mm, using the TOF + PSF method for both activity concentration ratios. Also, in Fig. 2b, the expected values of percentage of SUV_{max} difference (4 and 2) show that SUV_{max} was overestimated for all inserts except Φ10 mm for all the reconstruction methods.

Line profile of the hot inserts is shown in Fig. 3 The line profiles indicate that implementing the PSF and TOF algorithms within reconstruction steps creates a notable steep in the center of 37- and 22-mm cylindrical hot inserts, which is a result of signal enhancement in the edges due to Gibbs effect. In the line profile of the Φ37-mm insert reconstructed with TOF + PSF algorithm, the maximum activity concentration was 23.8 kBq/mL, corresponding to the edge of insert, while the minimum voxel value was in the center of insert (19.7 kBq/mL). So a rise of 21% was observed in the edge of the hot insert voxel values when using TOF + PSF algorithm. For smaller inserts, the Gibbs effect was seen as a peak in the center of the line profiles for the inserts of Φ10 mm and Φ17 mm. The line profile of the hot insert of Φ10 mm in the maximum values for the TOF + PSF method was about 30% higher than that of the OSEM algorithm.

Statistical analysis indicated that the median value of the relative difference of SNR was 107.1% ($p < 0.001$) for the
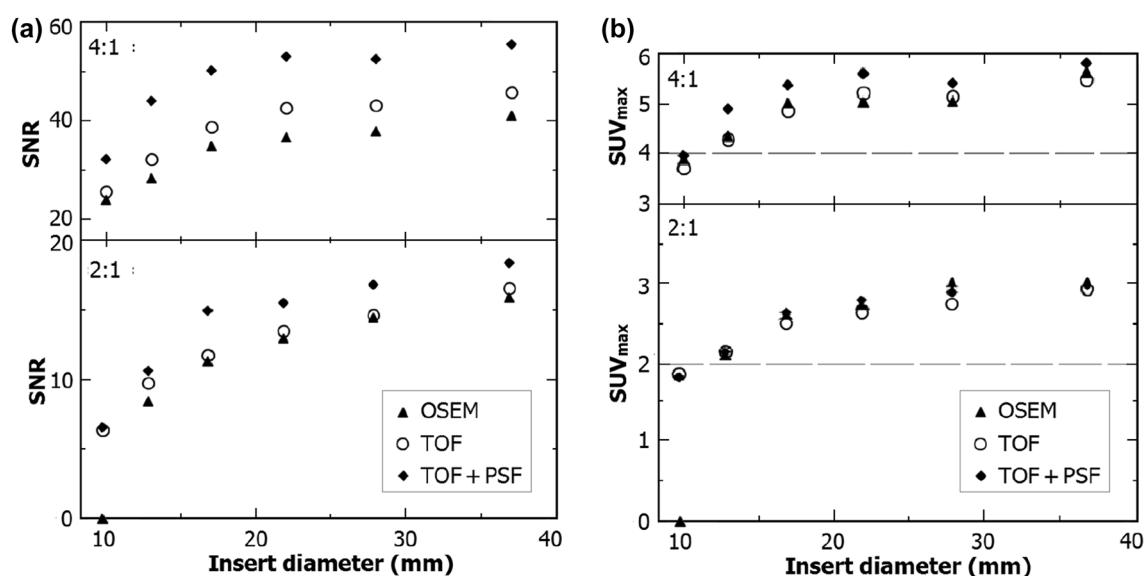

Fig. 2 SNR (**a**) and SUV_{max} (**b**) of the six inserts of image quality phantom for a LBR of 4:1 and 2:1

Table 2 ΔSNR for TOF and TOF + PSF images of the inserts, at activity concentration background of 5.3 kBq/mL, and ΔSUV$_{max}$ compared to OSEM

Phantom diameter (mm)	ΔSNR%						ΔSUV$_{max}$%			
	TOF		TOF + PSF		OSEM		TOF		TOF + PSF	
	2:1	4:1	2:1	4:1	2:1	4:1	2:1	4:1	2:1	4:1
10	NM	1.3	NM	27.9	NM	− 3	− 6.3	− 7.4	− 8.5	− 0.9
13	15.3	7.1	25.4	39.3	5	8.5	7.6	7.4	7.3	23.1
17	3.6	6.3	32.3	25.9	31.2	25.8	26.5	22.3	32.1	35.7
22	5.0	8.9	20.3	17.3	36.9	26.6	33.8	31.3	40.5	41.4
28	1.2	14.0	16.9	19.6	51.1	26.8	38.7	29.5	45.1	36.5
37	4.2	3.3	15.6	12.8	51.3	42.1	47.3	38.5	49.7	46.6

NM not measured
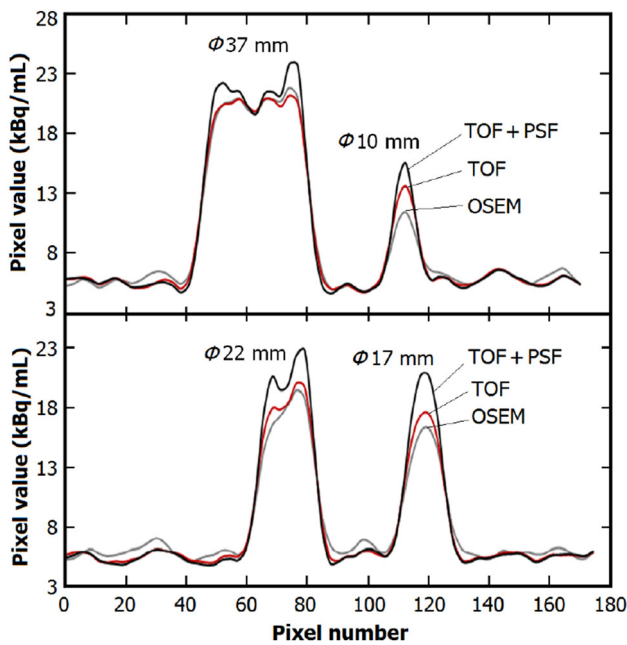
Fig. 3 Line profiles through cylindrical inserts of Φ10–37 mm for a LBR = 4:1

Fig. 4 Contrast changes of the detected lesions, as a function of lesion size, in PET images reconstructed with TOF and TOF + PSF method

TOF-to-OSEM methods and 28.8% ($p < 0.001$) for the TOF + PSF-to-OSEM methods. SNR gain was 1.6 ± 0.53 ($p < 0.001$) for the TOF-to-OSEM methods and 2.7 ± 0.74 ($p < 0.001$) for the TOF + PSF-to-OSEM methods.

Figure 4 shows the relative difference of lesion contrasts for the TOF and TOF + PSF algorithms, in comparison with the OSEM algorithm, as a function of lesion size. The effects of TOF and TOF + PSF algorithms were more significant for smaller lesions. To assess percentage changes in the contrast on lesion size, Spearman's correlation coefficient (SCC) was calculated for the TOF and TOF + PSF algorithms. The SCC for contrast changes with respect to lesion size was weak ($\rho = - 0.32$, $p = 0.008$) for TOF images, and moderate ($\rho = - 0.54$, $p < 0.0001$) for TOF + PSF images. The relative
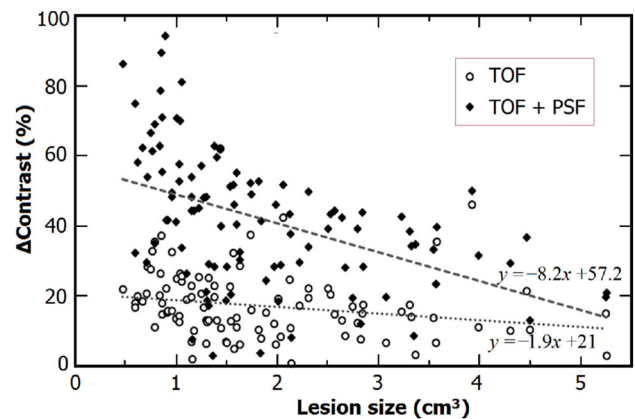
difference of contrast was $17 \pm 1.05\%$ ($p < 0.0001$) for the TOF-to-OSEM methods and $41.5 \pm 1.85\%$ ($p < 0.0001$) for the TOF + PSF-to-OSEM methods.

The agreement between SUV$_{max}$ of the OSEM algorithm and images reconstructed with the TOF and TOF + PSF methods was evaluated by Bland–Altman analysis (Fig. 5). SUV$_{max}$ for the TOF + PSF-to-OSEM methods (mean = 39.6%) was of higher bias than the TOF method (mean = 16.2%).

The impact of using various reconstruction methods for typical patient with gastric cancer is shown in Fig. 6. It is obvious that the TOF + PSF and TOF can generate higher SUVmax than the OSEM method, especially in small metastatic bone lesions.

4 Discussion

Image quality of the OSEM + TOF + PSF (TOF + PSF), OSEM + TOF (TOF), and OSEM algorithms in the new generation PET/CT scanner has been assessed quantitatively. Based on matched voxel noise
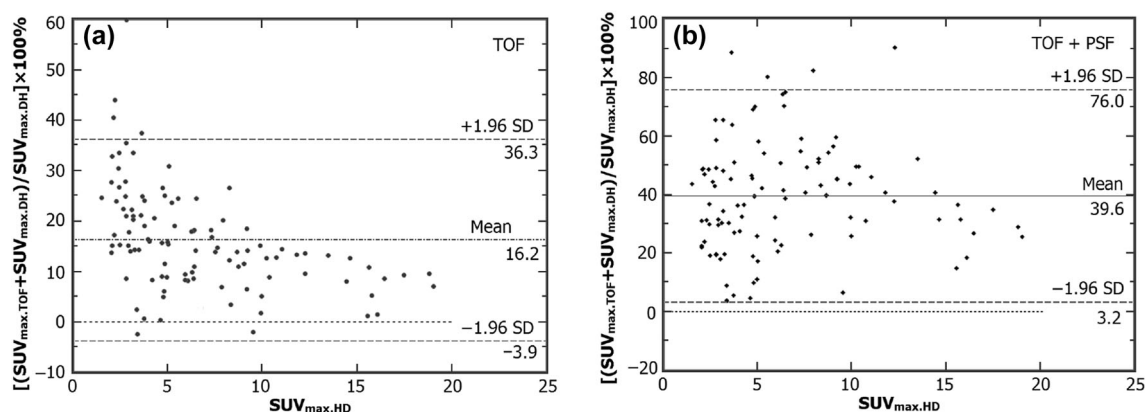
Fig. 5 Bland–Altman plot comparing the measured SUV_{max} differences of the TOF-to-OSEM (**a**) and TOF + PSF-to-OSEM (**b**)
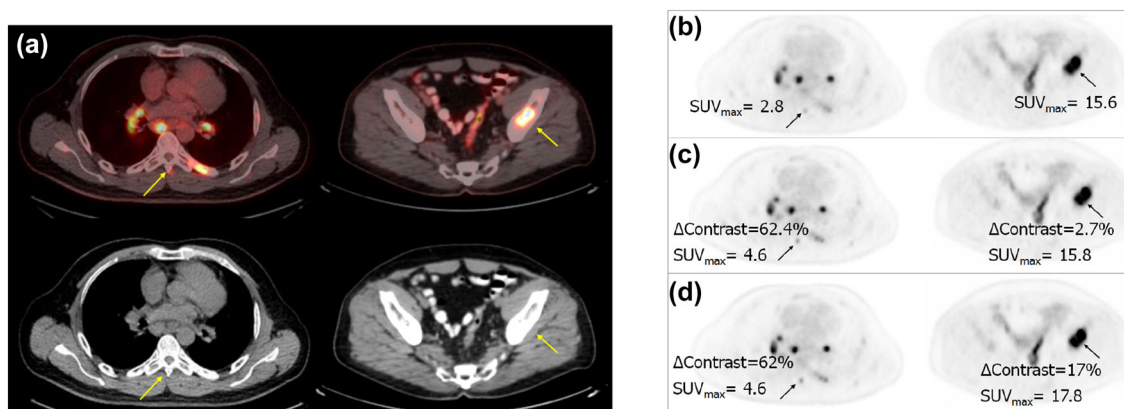

Fig. 6 Fused PET/CT images (**a**), PET images of a patient with gastric cancer reconstructed with the OSEM (**b**), TOF (**c**), and TOF + PSF method (**d**). Body weight: 88 kg, height: 175 cm, and injected dose: 414.4 MBq of ^{18}F-FDG

concept and our previous study (noise level below 10%) [27, 31], optimal reconstruction parameters (the number of iteration, subset, and FWHM of post-smoothing filter) were used in the phantom and clinical data. The noise level was $8.5 \pm 0.3\%$ for phantom images and $7.78 \pm 0.5\%$ for clinical data. The phantom study showed that applying the TOF algorithm can improve the image quality significantly for low uptake lesions, especially in small ones. This is in line with other studies [13, 37]. The TOF and PSF +TOF algorithms can improve lesion detectability for 10 mm hot insert at LBR = 2:1 by RC = 70.6 and 71.6%, respectively.

The TOF + PSF method enhances the recovery coefficient of activity concentration, with improved spatial resolution and signal improvement in all phantom images. In general, at the same noise level, the highest RC is observed for the TOF + PSF method, followed by the TOF and OSEM method. The PSF + TOF reconstruction has the highest SNR too, for all insert diameters and activity concentration ratios; however, the SNR gain is smaller for Φ22–37 mm inserts, and higher SNRs are observed for higher LBR. It was reported that TOF SNR was 1.4 times

higher than that of non-TOF images in patient study [18]. The TOF, and the TOF + PSF especially, can improve contrast and detectability of lesions, particularly small ones (< 2.20 cm^3).

Our phantom results verify high overestimation in SUV_{max} quantification even up to 49% for LBR = 4:1 and 2:1. Also, the PSF + TOF and TOF can increase of SUV_{max} in clinical PET/CT images. This is in line with previous studies [6, 25]. Previous studies also demonstrated that the PSF modeling by creating Gibbs artifact in parallel with partial volume effect correction contributed to the increase of SUV_{max} [38–41]. Thus, the SUV_{max} enhancement is greater using TOF + PSF. G. Akmatsu et al. reported that no significant difference was found between SUV_{max} of the conventional OSEM algorithm and TOF reconstruction for lymph node metastases [30]. The lack of statistical significance between the OSEM and TOF algorithm is probably due to selections of the reconstruction parameters including iteration, subset, and filter for both algorithms. In the other word, the reconstruction parameters for conventional algorithm can cause more noise level than to TOF images, and the presence of more noise in

conventional images increased the measured SUV_{max} in that study resulting the contradiction.

It is shown that the new advanced algorithms can improve image quality and lesion detectability. Quantification by SUV for determining lesion features highly depends on reconstruction algorithm, which should be considered for making clinical decision and diagnosis. Our investigation had some limitations. As BMI of the patients was smaller than 27 kg/m^2, heavy and obese patients were not evaluated in this study.

5 Conclusion

The TOF algorithm has the capability of providing better clinical image quality and detectability especially for small lesion with low uptake. At the same noise level, the combination of the PSF modeling with the TOF can give an improved image quality, due to improved SNR and contrast in PET images. The highest SUVmax was observed when implementing the TOF + PSF algorithm. It is also shown that the influence on image quality of using the TOF + PSF versus the TOF is more significant in small lesions with low uptake of ^{18}F-FDG. However, this influence decreased for larger lesions. In terms of quantification it is also shown that these algorithms affect the accuracy of measured SUVmax which can influence clinical decisions, and affect the assessment of response to therapy.

References

1. D. Delbeke, R.E. Coleman, M.J. Guiberteau et al., Procedure guideline for tumor imaging with 18F-FDG PET/CT 1.0. J. Nucl. Med. 47, 885–895 (2006). doi:10.1007/s00259-009-1297-4
2. W.A. Weber, Use of PET for monitoring cancer therapy and for predicting outcome. J. Nucl. Med. 46, 983–995 (2005)
3. C.J. Hoekstra, O.S. Hoekstra, S.G. Stroobants et al., Methods to monitor response to chemotherapy in non-small cell lung cancer with 18F-FDG PET. J. Nucl. Med. 43, 1304–1309 (2002)
4. D. Vriens, E.P. Visser, L.-F. de Geus-Oei et al., Methodological considerations in quantification of oncological FDG PET studies. Eur. J. Nucl. Med. Mol. Imaging 37, 1408–1425 (2010). doi:10.1007/s00259-009-1306-7
5. T. Beyer, J. Czernin, L.S. Freudenberg, Variations in clinical PET/CT operations: results of an international survey of active PET/CT users. J. Nucl. Med. 52, 303–310 (2011). doi:10.2967/jnumed.110.079624
6. G. Akamatsu, K. Ishikawa, K. Mitsumoto et al., Improvement in PET/CT image quality with a combination of point-spread function and time-of-flight in relation to reconstruction parameters. J. Nucl. Med. 53, 1716–1722 (2012). doi:10.2967/jnumed.112.103861
7. B. Knäusl, I. Rausch, H. Bergmann et al., Influence of PET reconstruction para meters on the TrueX algorithm. Nuklearmedizin (2012). doi:10.3413/Nukmed-0523-12-07

8. G. Kuhnert, R. Boellaard, S. Sterzer et al., Impact of PET/CT image reconstruction methods and liver uptake normalization strategies on quantitative image analysis. Eur. J. Nucl. Med. Mol. 43, 249–258 (2016). doi:10.1007/s00259-015-3165-8
9. S. Sheikhbahaei, C. Marcus, R. Wray et al., Impact of point spread function reconstruction on quantitative 18F-FDG-PET/CT imaging parameters and inter-reader reproducibility in solid tumors. Nucl. Med. Commun. 37, 288–296 (2016). doi:10.1097/MNM.0000000000000445
10. W. Moses, Time of flight in PET revisited. IEEE Trans. Nucl. Sci. 50, 1325–1330 (2003). doi:10.1109/TNS.2003.817319
11. S. Tong, A. Alessio, P. Kinahan, Noise and signal properties in PSF-based fully 3D PET image reconstruction: an experimental evaluation. Phys. Med. Biol. 55, 1453–1473 (2010). doi:10.1088/0031-9155/55/5/013
12. S. Surti, J.S. Karp, L.M. Popescu et al., Investigation of time-of-flight benefit for fully 3-DPET. IEEE Trans. Med. Imaging 25, 529–538 (2006). doi:10.1088/0031-9155/58/5/1465
13. J. Schaefferkoetter, M. Casey, D. Townsend et al., Clinical impact of time-of-flight and point response modeling in PET reconstructions: a lesion detection study. Phys. Med. Biol. 58, 1465–1478 (2013). doi:10.1088/0031-9155/58/5/1465
14. M. Conti, B. Bendriem, M. Casey et al., First experimental results of time-of-flight reconstruction on an LSO PET scanner. Phys. Med. Biol. 50, 4507–4526 (2005). doi:10.1088/0031-9155/50/19/006
15. V.Y. Panin, F. Kehren, C. Michel et al., Fully 3-D PET reconstruction with system matrix derived from point source measurements. IEEE Trans. Med. Imaging 25, 907–921 (2006). doi:10.1109/TMI.2006.876171
16. A.M. Alessio, C.W. Stearns, S. Tong et al., Application and evaluation of a measured spatially variant system model for PET image reconstruction. IEEE Trans. Med. Imaging 29, 938–949 (2010). doi:10.1109/TMI.2010.2040188
17. A. Varrone, N. Sjöholm, L. Eriksson et al., Advancement in PET quantification using 3D-OP-OSEM point spread function reconstruction with the HRRT. Eur. J. Nucl. Med. Mol. Imaging 36, 1639–1650 (2009). doi:10.1007/s00259-009-1156-3
18. C. Lois, B.W. Jakoby, M.J. Long et al., An assessment of the impact of incorporating time-of-flight information into clinical PET/CT imaging. J. Nucl. Med. 51, 237–245 (2010). doi:10.2967/jnumed.109.068098
19. D.J. Kadrmas, M.E. Casey, M. Conti et al., Impact of time-of-flight on PET tumor detection. J. Nucl. Med. 50, 1315–1323 (2009). doi:10.2967/jnumed.109.063016
20. J.S. Karp, S. Surti, M.E. Daube-Witherspoon et al., Benefit of time-of-flight in PET: experimental and clinical results. J. Nucl. Med. 49, 462–470 (2008). doi:10.2967/jnumed.107.044834
21. S. Surti, J. Scheuermann, G. El Fakhri et al., Impact of time-of-flight PET on whole-body oncologic studies: a human observer lesion detection and localization study. J. Nucl. Med. 52, 712–719 (2011). doi:10.2967/jnumed.110.086678
22. M. Conti, Focus on time-of-flight PET: the benefits of improved time resolution. Eur. J. Nucl. Med. Mol. Imaging 38, 1147–1157 (2011). doi:10.1007/s00259-010-1711-y
23. G. El Fakhri, S. Surti, C.M. Trott et al., Improvement in lesion detection with whole-body oncologic time-of-flight PET. J. Nucl. Med. 52, 347–353 (2011). doi:10.2967/jnumed.110.080382
24. V. Bettinardi, L. Presotto, E. Rapisarda et al., Physical performance of the new hybrid PET/CT discovery-690. Med. Phys. 38, 5394–5411 (2011). doi:10.1118/1.3635220
25. B. Jakoby, Y. Bercier, M. Conti et al., Physical and clinical performance of the mCT time-of-flight PET/CT scanner. Phys. Med. Biol. 56, 2375–2389 (2011). doi:10.1088/0031-9155/56/8/004

26. B. Jakoby, Y. Bercier, M. Conti et al., *Performance investigation of a time-of-flight PET/CT scanner* (Sci. Conf. R., IEEE Nucl, 2008). doi:10.1109/NSSMIC.2008.4774221

27. M. Shekari, P. Ghafarian, S. Ahangari et al., Optimizing image reconstruction parameters in time of flight PET/CT imaging: a phantom study. Front. Biomed. Technol. **2**, 146–154 (2015)

28. S. Ahangari, P. Ghafarian, M. Shekari et al., The impact of point spread function modeling on scan duration in PET imaging. Front. Biomed. Technol. **2**, 137–145 (2015)

29. E. Prieto, I. Domínguez-Prado, M.J. García-Velloso et al., Impact of time-of-flight and point-spread-function in SUV quantification for oncological PET. Clin. Nucl. Med. **38**, 103–109 (2013). doi:10.1097/RLU.0b013e318279b9df

30. G. Akamatsu, K. Mitsumoto, T. Taniguchi et al., Influences of point-spread function and time-of-flight reconstructions on standardized uptake value of lymph node metastases in FDG-PET. Eur. J. Radiol. **83**, 226–230 (2014). doi:10.1016/j.ejrad.2013.09.030

31. I.S. Armstrong, M.D. Kelly, H.A. Williams et al., Impact of point spread function modelling and time of flight on FDG uptake measurements in lung lesions using alternative filtering strategies. EJNMMI Phys. **1**, 99 (2014)

32. N. Paquet, A. Albert, J. Foidart, R. Hustinx, Within-patient variability of ^{18}F-FDG: standardized uptake values in normal tissues. J. Nucl. Med. **45**, 784–788 (2004)

33. R. Boellaard, R. Delgado-Bolton, W.J. Oyen et al., FDG PET/CT: EANM procedure guidelines for tumour imaging: version 2.0. Eur. J. Nucl. Med. Mol. Imaging **42**, 328–354 (2015). doi:10.1007/s00259-014-2961-x

34. C.W. Stearns, D.L. McDaniel, S.G. Kohlmyer et al., Random coincidence estimation from single event rates on the discovery ST PET/CT scanner. IEEE Nucl. Sci. Conf. R. (2003). doi:10.1109/NSSMIC.2003.1352545

35. M. Iatrou, R. Manjeshwar, S. Ross et al., 3D implementation of scatter estimation in 3D PET. IEEE Nucl. Sci. Conf. R. **4**, 2142–2145 (2006). doi:10.1109/NSSMIC.2006.354338

36. T.L. Morgan, Quality assurance for PET and PET/CT systems. Health Phys. **103**, 810–811 (2012). doi:10.1097/HP.0b013e3182690427

37. H. Tsuru et al., Time-of-flight information improves the detectability of sub-centimeter lesions using clinical PET/CT system. J. Nucl. Med. **57**(Supplement 2), 2686 (2016)

38. F.L. Andersen, T.L. Klausen, A. Loft et al., Clinical evaluation of PET image reconstruction using a spatial resolution model. Eur. J. Radiol. **82**, 862–869 (2013). doi:10.1016/j.ejrad.2012.11.015

39. C. Lasnon, R.J. Hicks, J.-M. Beauregard et al., Impact of point spread function reconstruction on thoracic lymph node staging with ^{18}F-FDG PET/CT in non-small cell lung cancer. Clin. Nucl. Med. **37**, 971–976 (2012). doi:10.1097/RLU.0b013e318251e3d1

40. B. Bai, P.D. Esser, The effect of edge artifacts on quantification of positron emission tomography. IEEE Nucl. Sci. Symp. Med. Imaging Conf. (2010). doi:10.1109/NSSMIC.2010.5874186

41. D. Kidera, K. Kihara, G. Akamatsu et al., The edge artifact in the point-spread function-based PET reconstruction at different sphere-to-background ratios of radioactivity. Ann. Nucl. Med. **30**, 97–103 (2016). doi:10.1007/s12149-015-1036-9